



ELSEVIER

Parallel Computing 23 (1997) 1235–1248

PARALLEL
COMPUTING

Parallel 3D computation of unsteady flows around circular cylinders

V. Kalro ^{*}, T. Tezduyar ¹

*Department of Aerospace Engineering and Mechanics, Army High Performance Computing Research Center,
University of Minnesota, 1100 Washington Avenue South, Minneapolis, MN 55415, USA*

Received 22 August 1996; revised 18 February 1997

Abstract

In this article we present parallel 3D finite element computation of unsteady incompressible flows around circular cylinders. We employ stabilized finite element formulations to solve the Navier–Stokes equations on a thinking machine CM-5 supercomputer. The time integration is based on an implicit method, and the coupled, nonlinear equations generated every time step are solved iteratively, with an element-vector based evaluation technique. This strategy enables us to carry out these computations with millions of coupled, nonlinear equations, and thus resolve the flow features in great detail. At Reynolds number 300 and 800, our results indicate strong 3D features arising from the instability of the columnar vortices forming the Karman street. At $Re = 10\,000$ we employ a large eddy simulation (LES) turbulence model. © 1997 Elsevier Science B.V.

Keywords: Large-scale problems; Parallel computations; 3D cylinder flows; LES

1. Introduction

Large-scale flow simulations have reached to levels unimaginable only a decade ago, owing to the major advances in high performance computing (HPC) technology. Modern supercomputing platforms harness hundreds of widely available computer chips to provide tremendous resources both in terms of raw computing power and memory. These workhorses are aptly termed massively parallel processors (MPP). It is believed that in the near future these machines will be capable of sustaining TeraFLOPs performance.

^{*} Corresponding author. Tel.: +1-612-6268096; fax: +1-612-6261596; e-mail: kalro@ahpcrc.umn.edu.

¹ E-mail: tezduyar@ahpcrc.umn.edu.

The programming style on MPPs varies extensively from machine to machine, thus, advances in development of efficient parallel algorithms are vital for optimal utilization of the new HPC technology. A single-instruction-multiple-data (SIMD) style of programming within a data parallel paradigm is described in Behr et al. [1]. A number of flow simulations using related finite element techniques were reported recently [2–6]. Simulations utilizing multiple-instruction-multiple-data (MIMD) programming styles are presented in Refs. [7,8]. Our computations here are based on stabilized finite element formulations, which were described earlier [5]. These stabilized techniques [9,10] suppress the numerical oscillations in the field variables by introducing minimal numerical diffusion while maintaining consistency in the sense that the stabilizers are weighted residuals of the governing equations. The coupled, nonlinear equations generated at every time step are solved iteratively, with GMRES [11] update technique; and by computing the residuals based on matrix-free (element-vector based) evaluations.

While the new technology has empowered us to attempt very large-scale simulations around fairly complex geometries, the issue of turbulence is yet to be completely resolved. With direct numerical simulation (DNS), even the most powerful machines available today can handle only very moderate Reynolds numbers. Thus one has to resort to turbulence models to account for the subgrid-scale structures in the flow. In this paper the Smagorinsky [12] large eddy simulation (LES) model is used to represent the turbulence effects. This model is used here in its simplest form with a constant coefficient (the interested reader is referred to Germano [13] and Moin [14] for discussions on more sophisticated dynamic subgrid-scale models).

We present 3D finite element computation of unsteady incompressible flows around a classical geometry, namely the circular cylinder. These flows are studied for a number of reasons. Firstly, a large amount of experimental data is available for the cylinder; this aids in validating the accuracy of the formulations and the various modeling assumptions. Secondly, although this geometry is simple, the associated flow fields are enriched with fundamental phenomena which form the building blocks of more complex flows. Hence, base flows like these continue to attract the attention of fluid mechanics researchers.

Until recently most numerical simulations have been restricted to 2D cases (see Mittal [15] for example) due to lack of computational power, whereas, experiments reported indicate the presence of strong 3D features above $Re \sim 200$. Recently there has been renewed interest in the 3D nature of the cylinder wake [16–18]. With the HPC tools we now possess, it is possible to resolve the flow features at moderately large Reynolds numbers with sufficient detail. We investigate the unsteady flows past a stationary cylinder at Reynolds number 300 and 800. At $Re = 10\,000$, our simulation is based on the LES model mentioned above.

All simulations are computed on the thinking machine CM-5.

2. 3D flows at low Reynolds numbers

At low Reynolds numbers one observes symmetric attached eddies aft of the cylinder. At around $Re = 40$, the wake becomes unstable and begins to oscillate. These oscillations roll up into discrete vortices which are periodically shed when $Re > 60$. This

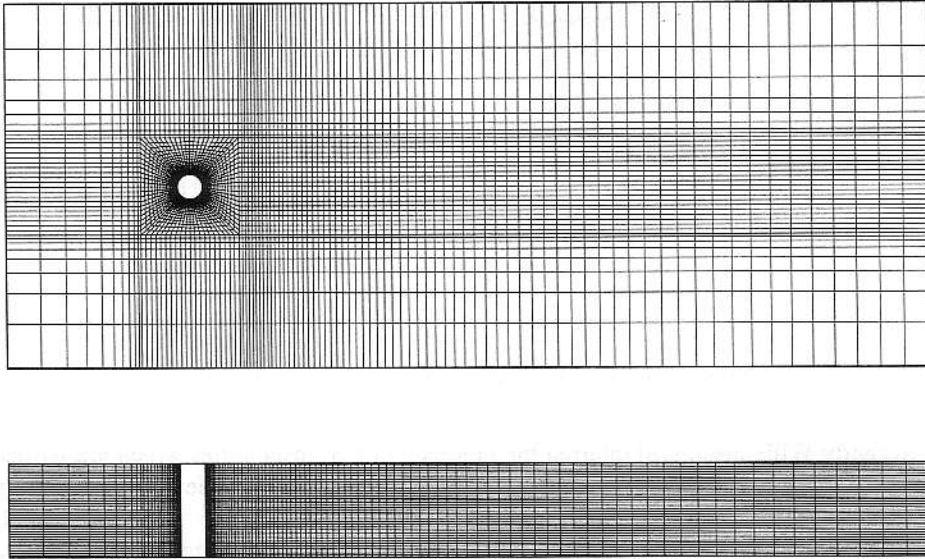


Fig. 1. Mesh for computing flow at $Re = 300$ and 800 (197 948 nodes and 186 240 elements) ($x-y$ plane in top image and $x-z$ plane in bottom image).

uniformly spaced trail of vortices is referred to as the Karman vortex street. Roshko [19] first reported a detailed measurement of the Strouhal number corresponding to the vortex shedding for a wide range of Reynolds numbers. Since then researchers have reported frequencies which differ as much as 20%; further, a discontinuity in the $St-Re$ correlation has also been recorded. Williamson [20] attributes these findings to the boundary conditions at the cylinder ends, and the 3D effects which appear at $Re \sim 190$. He observed both oblique and parallel vortex shedding modes, depending on whether the central flow could match up with the end conditions. By using endplates, he was able to coerce the flow to obtain parallel vortex shedding.

In simulations discussed here, the cylinder spans the entire crossflow domain, and the boundary conditions used enforce parallel shedding. Computations at $Re = 300$ and 800 were performed on a mesh of hexahedral elements (see Fig. 1). The diameter of the cylinder is 2 units and the length is 8 units (this length was chosen after some trials so as to capture a few wavelengths along the cylinder axis). The mesh extends 15 units upstream, 60 units downstream, and 30 units in the crossflow direction. The mesh consists of 186 240 elements (4656 elements in a 2D section, 40 along the span of the cylinder and 80 along its circumference) and 197 948 nodes, and results in 760 107 equations. The radial thickness of the first layer of elements is 0.01 units. The boundary conditions consist of uniform inflow velocity, zero-normal-velocity and zero-shear-stress at the lateral boundaries, traction-free conditions at the outflow boundary, and no-slip on the cylinder.

For these simulations the time step is set to 0.05 and the inflow velocity to 1.0. The number of nonlinear iterations at each time step is 3, and the size of the Krylov space is 10, with no restarts. These computations require 13.7 s/time step on a 256-PN CM-5.

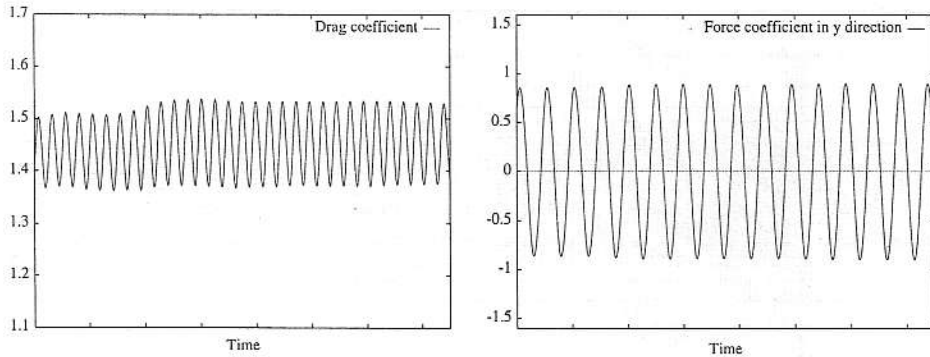


Fig. 2. Flow at $Re = 300$: time-histories of the force coefficients.

Recently Williamson [18] inferred the presence of two instabilities which are termed mode A (appearing at $Re \sim 190$) and mode B (at $Re \sim 260$). In mode A, the instability arises due to the amplification of spanwise disturbances by the strain rate fields surrounding the vortex cores. In mode B, the structures arise from instabilities associated with the vorticity layer between successive cores. The mode A instability is marked by streamwise loops of vorticity of wavelength $\sim 4.0D$; the mode B instability is comprised of strands of streamwise vortex pairs with characteristic wavelength $\sim 1.0D$, where D is the cylinder diameter. The value for Strouhal number from present computations and the topology of the wake structure at $Re \sim 300$ resembles mode B.

2.1. Flow at $Re = 300$

This computation was advanced in time until it was observed that the spatially-averaged aerodynamic coefficients reached a periodic state (see Fig. 2). Comparisons are made with time-histories of force coefficients obtained from 2D simulation (see Fig. 3) over a time interval spanning 1500 time steps. The agreement between 2D and 3D simulations is good since the 3D features are weak and the vortex axes are nearly aligned with the cylinder axis in the near wake. The Strouhal number from the 2D

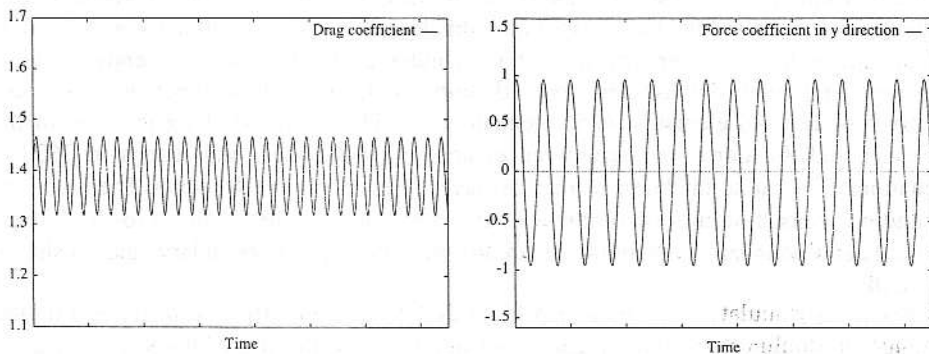


Fig. 3. Flow at $Re = 300$: time-histories of the force coefficients from 2D simulations.

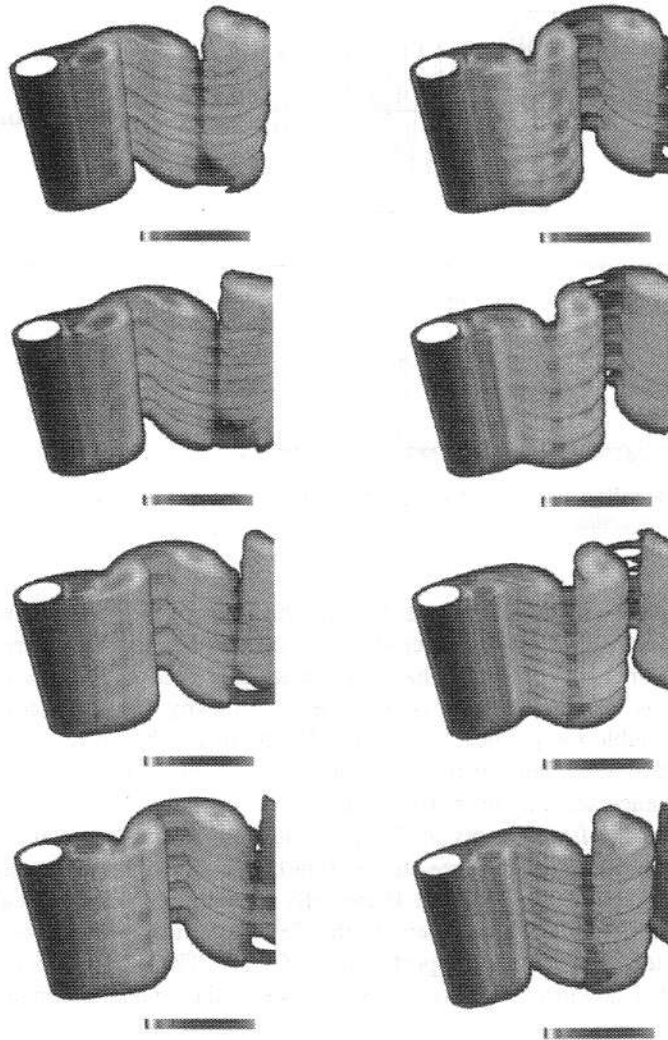


Fig. 4. Flow at $Re = 300$: magnitude of the vorticity at equally spaced instants during a shedding period (frames 1, 2, 3, 4 on the left and 5, 6, 7, 8 on the right).

simulation is 0.202. In the 3D simulation, a Karman vortex street is observed in the periodic state, and the corresponding Strouhal number is 0.203 (experiments ~ 0.2).

Visualization of the vorticity isosurfaces (see Fig. 4) shows the separated shear layer with the appearance of secondary instabilities in the form of spanwise waves. Approximately 4–5 waves are captured with the present mesh. These waves increase in amplitude downstream, resulting in the release of wavy columnar vortices. The frames taken at different instants during a shedding period reveal the process of vortex formation and associated instabilities.

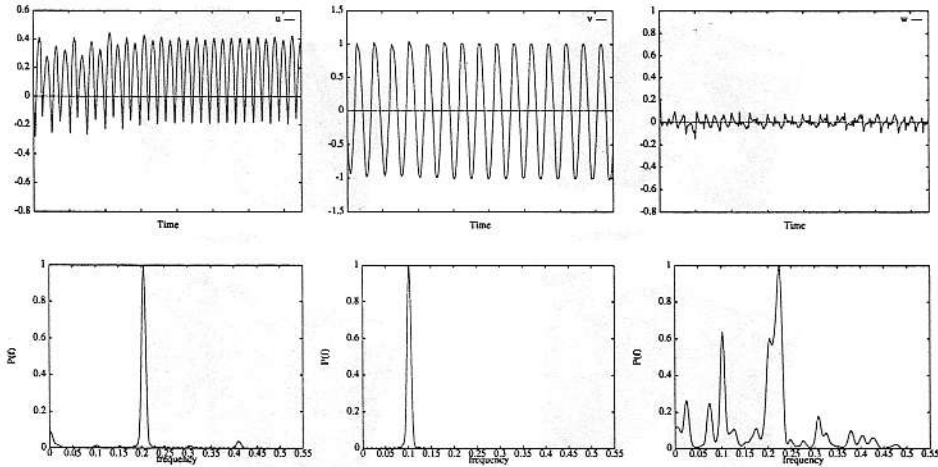


Fig. 5. Flow at $Re = 300$: time-histories and power spectra of 'u', 'v', 'w' at a point downstream of the cylinder along the centerline.

To get a measure of the 3D effects, the time-histories of the velocity and pressure at 2.85 units downstream of the cylinder along the centerline (see Fig. 5) are traced. Note that the 'v' component of velocity has a frequency half that of 'u' which is due to the alternating signs of vortices (this is also the reason why the force coefficient in y direction has double the period of the drag). Furthermore, the power spectra show the existence of two dominant frequencies for 'w'; one of them corresponding to the shedding frequency and the other twice that.

Fig. 6 shows the flow vectors in different spanwise planes (parallel to the cylinder axis and perpendicular to the free-stream flow). We can observe the appearance of regularly spaced cells at $x/d = 4.60$. These cells are split into pairs of weak streamwise counter-rotating vortices. These resemble the Taylor vortices seen between concentric rotating cylinders and are also reported in Ref. [21]. The wake structure retains its regularity further downstream ($x/d = 6.85$), however the cells are elongated, plausibly

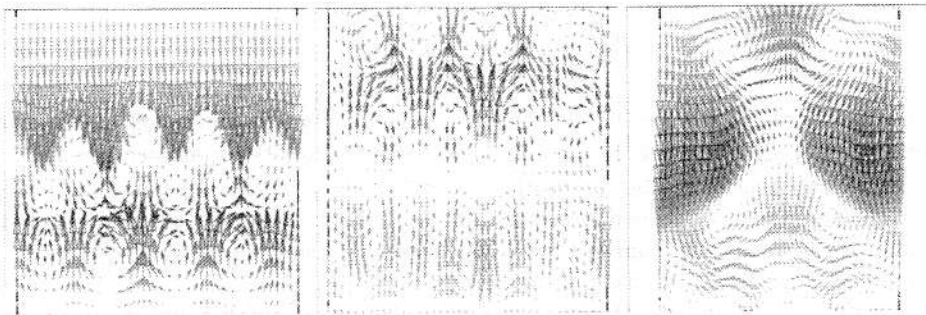


Fig. 6. Flow at $Re = 300$: velocity vectors in spanwise planes at $x/d = 4.60$ (left), 6.85 (center), 11.36 (right).

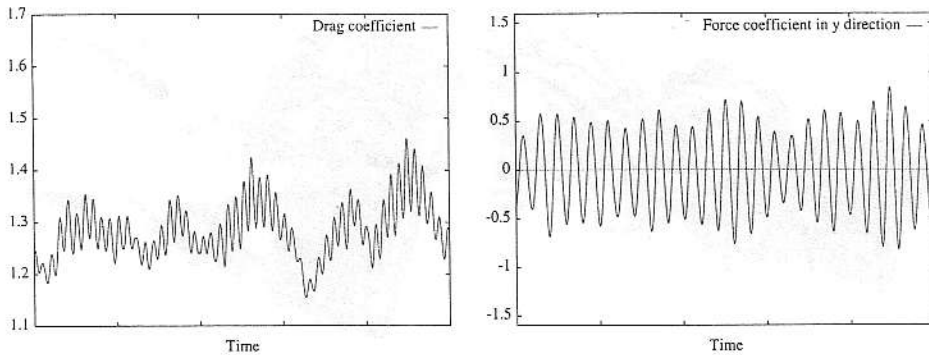


Fig. 7. Flow at $Re = 800$: time-histories of the force coefficients.

due to the widening distance between the vortex cores. Further downstream at $x/d = 11.36$ the wake structure is quite different and one can observe the arrangement of streamwise vortices in a 'cross' formation.

2.2. Flow at $Re = 800$

The time-histories of the force coefficients for this case are shown in Fig. 7. These are no longer uniform as those measured at $Re = 300$. 3D features are stronger. The time-histories of the force coefficients are compared over 2500 time steps with those obtained from 2D simulation (Fig. 8). Since at higher Reynold numbers the boundary layer is sharper, the velocity gradients are larger, resulting in the release of stronger vortices. As a result, the amplitudes of the force coefficients for the 2D simulation are larger than those at $Re = 300$. However this is not seen in the 3D simulation since the vortices are significantly distorted and possess components besides that in the spanwise direction. The Strouhal number from 2D simulation is 0.217, this is higher than that reported in experiments (~ 0.2).

Fig. 9 shows the isosurfaces for two different vorticity values. There is a breakdown

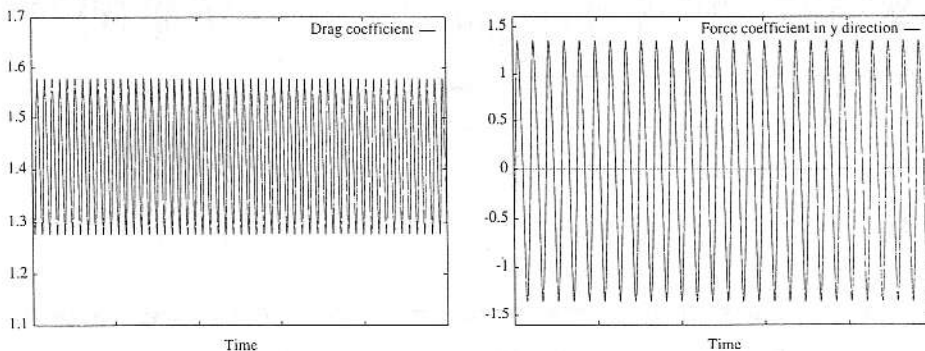


Fig. 8. Flow at $Re = 800$: time-histories of the force coefficients from 2D simulation.

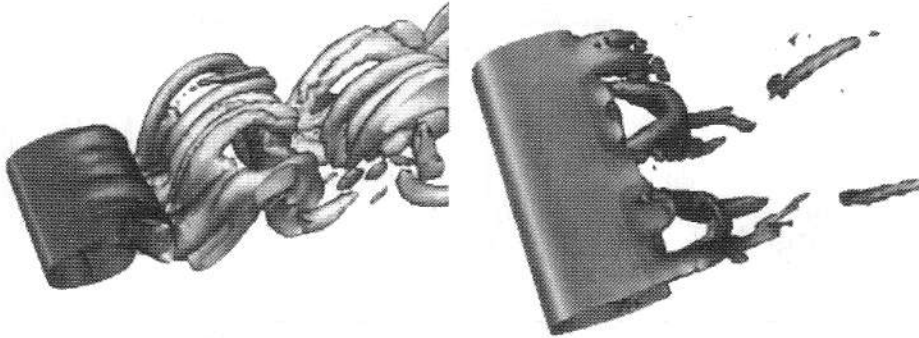


Fig. 9. Flow at $Re = 800$: vorticity isosurfaces for $|\omega| = 0.5$ (left) and 2.0 (right).

in the regular spanwise structure observed at $Re = 300$. We can also observe distinct strands of streamwise vorticity ($|\omega| = 0.5$). In the right image the distortion of spanwise vortex cores to form loops is observed.

The increased 3D effects are also indicated by the 'w' component of velocity (see Fig. 10). The power spectra of 'w' indicates the existence of multiple peaks. However the dominant frequency in the spectra still corresponds to the vortex shedding frequency. The presence of a peak at a frequency half that of the dominant frequency is also observed. The Strouhal number corresponding to the shedding frequency is 0.203 and agrees well with experiment.

Fig. 11 shows instantaneous velocity vectors in spanwise planes in the vicinity of $x/d = 1.24$. The presence of counter-rotating streamwise vortex pairs is seen. However these vortex pairs are not arranged in a regular fashion. They merge together and cancel

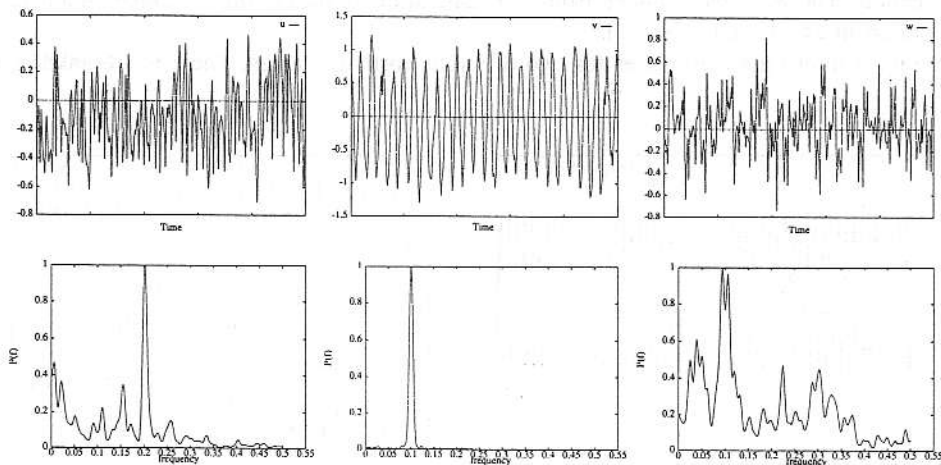


Fig. 10. Flow at $Re = 800$: time-histories and power spectra of 'u', 'v', 'w' at a point downstream of the cylinder along the centerline.

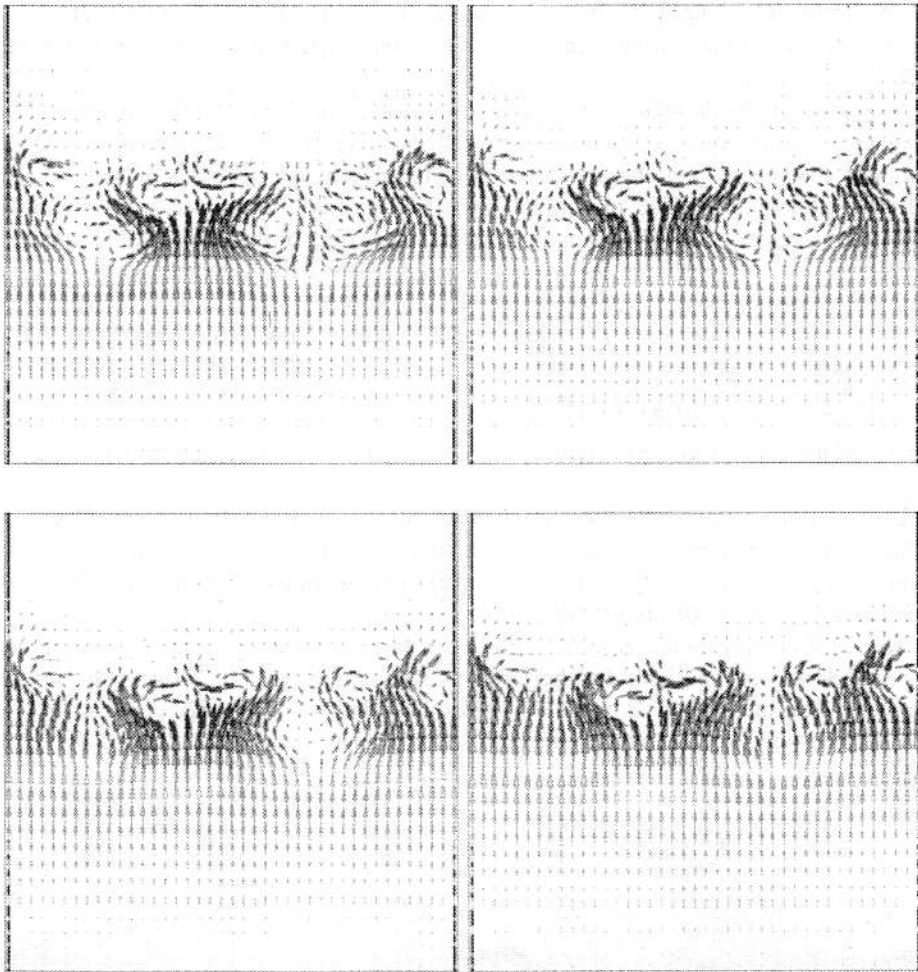


Fig. 11. Flow at $Re = 800$: velocity vectors in spanwise planes $x/d = 1.15$ (top left), 1.19 (top right), 1.26 (bottom left), 1.33 (bottom right). Observe the annihilation of the counter-rotating vortex pair to the right of center.

each other. These ‘mushroom’ shaped vortex pairs are characteristics of turbulent flow regions.

3. LES of flow around a cylinder at $Re = 10\,000$

As the Reynolds number increases, entities with diminishing scales appear in the flow. If one desires to capture all the flow details without any modification of the formulations, very fine grids need to be utilized. An approximation to the number of grid points required is given by $\sim Re^{2.25}$. This comes from the requirement of resolving

the Kolmogoroff scale (which is the scale at which all the turbulent energy is dissipated). An estimate of this scale based on dimensional analysis, is discussed in Ref. [22].

Numerical methods which attempt to resolve the fine features without any special treatment (except mesh refinement) are called direct numerical simulations (DNS). Although the supercomputing architectures of today provide gigabytes of memory, this is barely sufficient for DNS of simple flows. Hence, one often resorts to resolving the large-scale features of the flow, and representing the effect of the unresolvable scales via turbulence models. This is precisely the philosophy behind LES models. In this class of methods, spatial filtering is applied to the Navier–Stokes equations, and a Smagorinsky model is used to represent the subgrid-scale eddies. This results in the localized modification of the effective viscosity:

$$\nu_{\text{sgs}} = (C_s h)^2 \sqrt{2 \boldsymbol{\varepsilon}(\mathbf{u}) : \boldsymbol{\varepsilon}(\mathbf{u})}, \quad (1)$$

where $\boldsymbol{\varepsilon}(\mathbf{u})$ is the strain rate tensor, $C_s = 0.15$, and h is the representative element length.

LES is unlike Reynolds averaged Navier–Stokes (RANS) simulations where the entire range of turbulence scales is modeled [14] and only mean flow features are resolved. LES simulations typically require finer grids than RANS computations and are able to capture the unsteady turbulent effects.

The LES computations presented here were carried out on a mesh with the dimensions the same as those used for the previous simulations. Fig. 12 shows two views of the mesh. This mesh consists of 1 177 600 hexahedral elements (14 720 elements in a 2D section, 80 along the cylinder span and 160 along its circumference) and 1 213 056

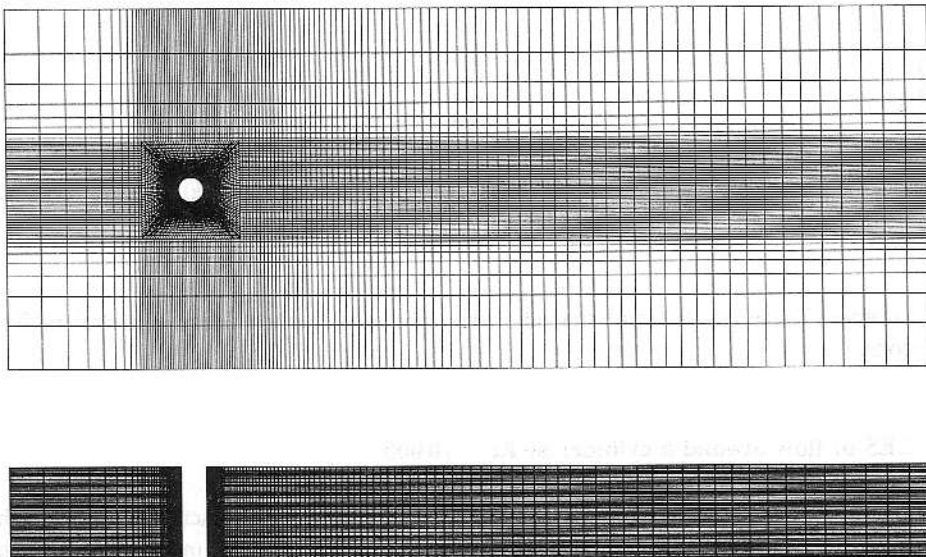


Fig. 12. Mesh for computing flow at $Re = 10000$ (1 213 056 nodes and 1 177 600 elements) ($x-y$ plane in top image and $x-z$ plane in bottom image).

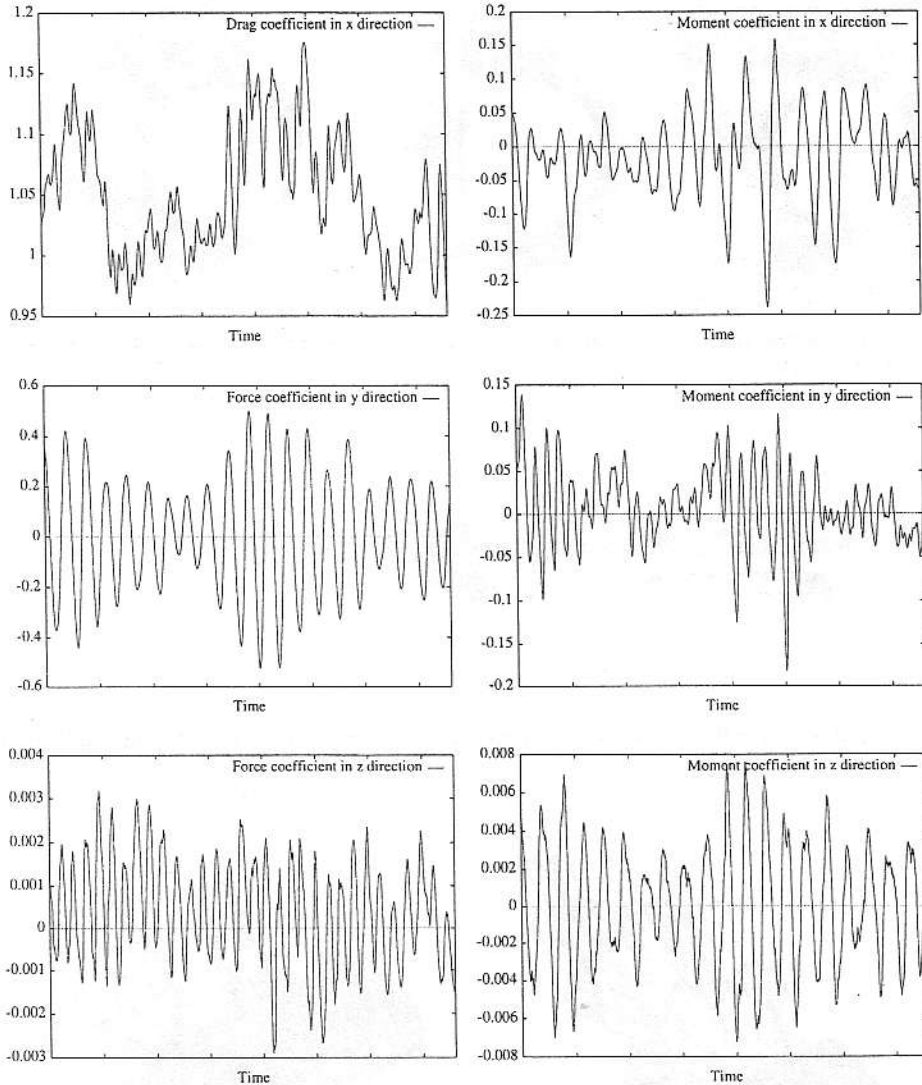


Fig. 13. LES of flow at $Re = 10,000$: time-histories of the aerodynamic coefficients.

nodes, and results in 4750535 equations. The radial thickness of the layer of elements along the cylinder is 0.001. Boundary conditions are the same as the two lower Reynolds number cases.

The inflow velocity is set to 1.0, time step to 0.025, and the Krylov space to 15 with no restarts. Two nonlinear iterations are performed at every time step. Computations proceeded at 37.7 s/time step on a 512-PN CM-5.

Since a 3D computation on such a fine mesh is costly, an initial condition was generated by projecting a 2D unsteady solution computed on a spanwise section (with

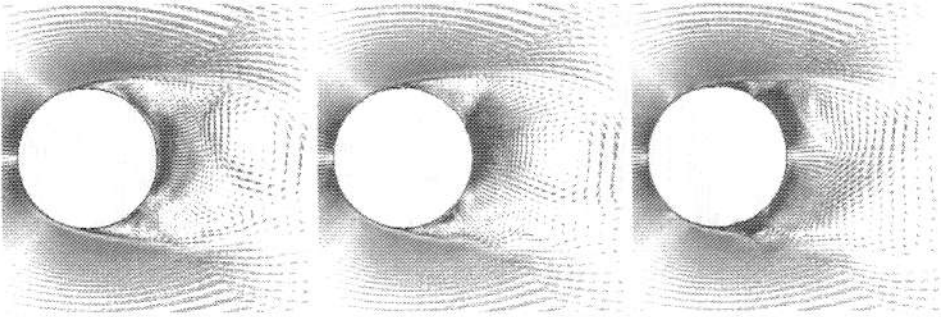


Fig. 14. LES of flow at $Re = 10,000$: velocity vectors in the chordwise planes at $z/d = -4.00$ (left), -1.75 (center), 4.00 (right).



Fig. 15. LES of flow at $Re = 10,000$: velocity vectors in spanwise planes at $x/d = 0.96$ (left), 1.24 (center), 4.80 (right).

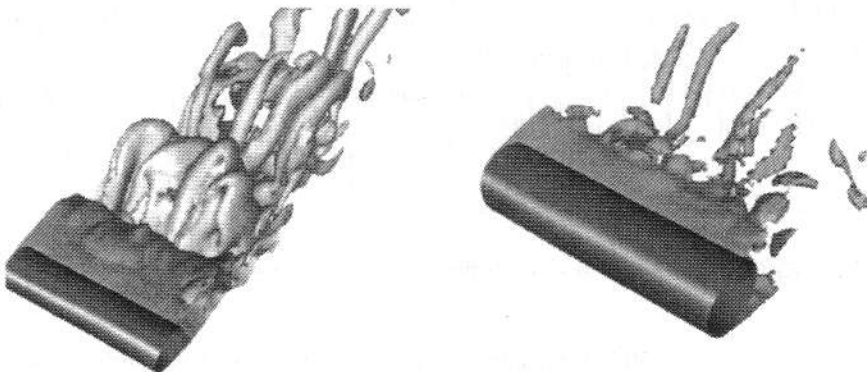


Fig. 16. LES of flow at $Re = 10,000$: vorticity isosurfaces for $|\omega| = 0.5$ (left) and 2.0 (right).

14720 elements) of the 3D mesh. Fig. 13 shows the time-histories of the force and moment coefficients over 4000 time steps. The time-averaged drag coefficient is 1.05 and compares well with experiment [23] (~ 1.12). The Strouhal number is 0.204 and also concurrent with experimental measurements [24] (~ 0.2).

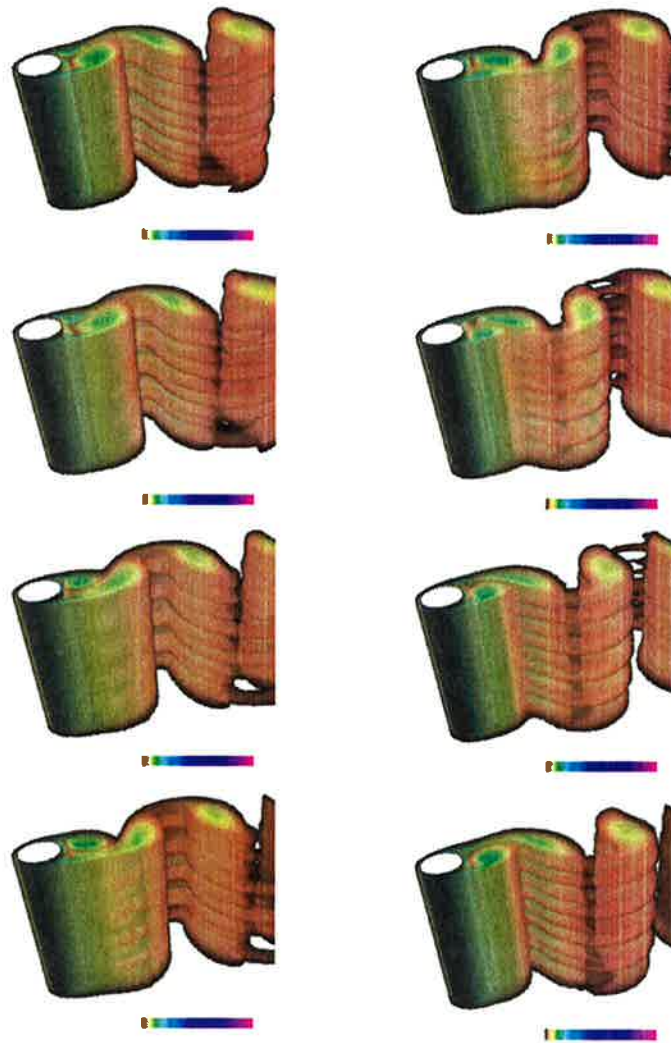


Figure 4. Flow at $Re = 300$: magnitude of the vorticity at equally spaced instants during a shedding period (frames 1, 2, 3, 4 on the left and 5, 6, 7, 8 on the right).

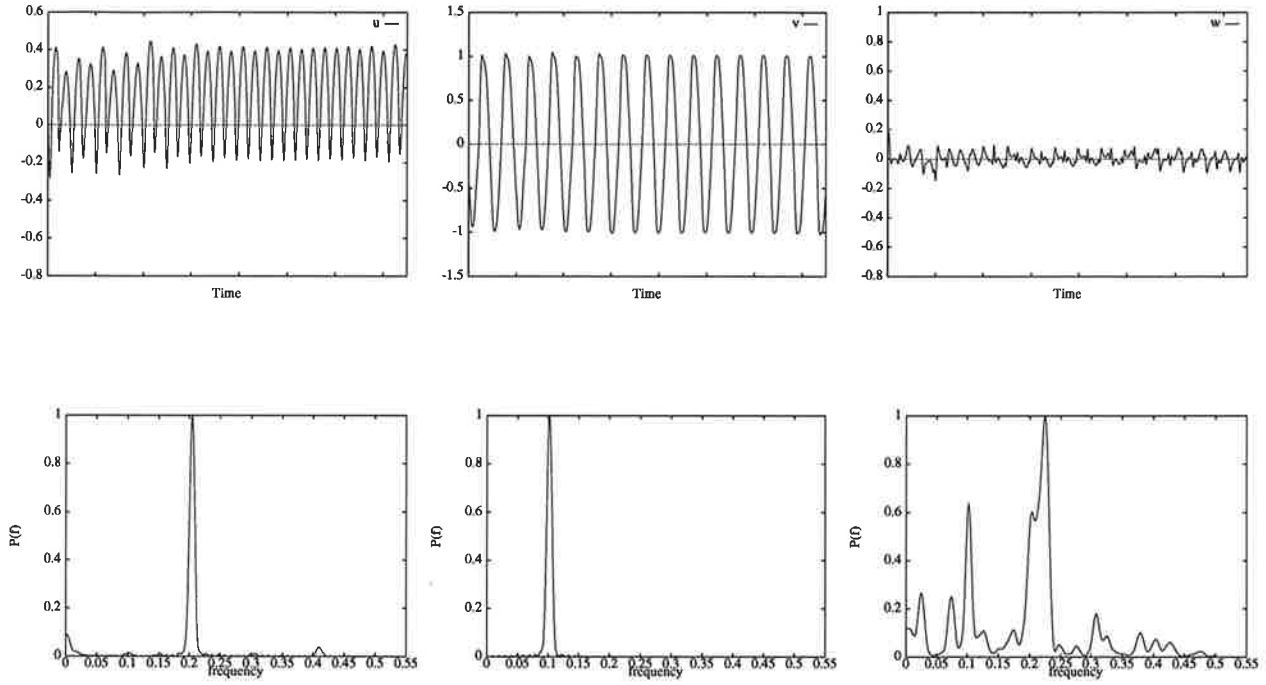


Figure 5. Flow at $Re = 300$: time-histories and power spectra of ' u ', ' v ', ' w ' at a point downstream of the cylinder along the centerline.

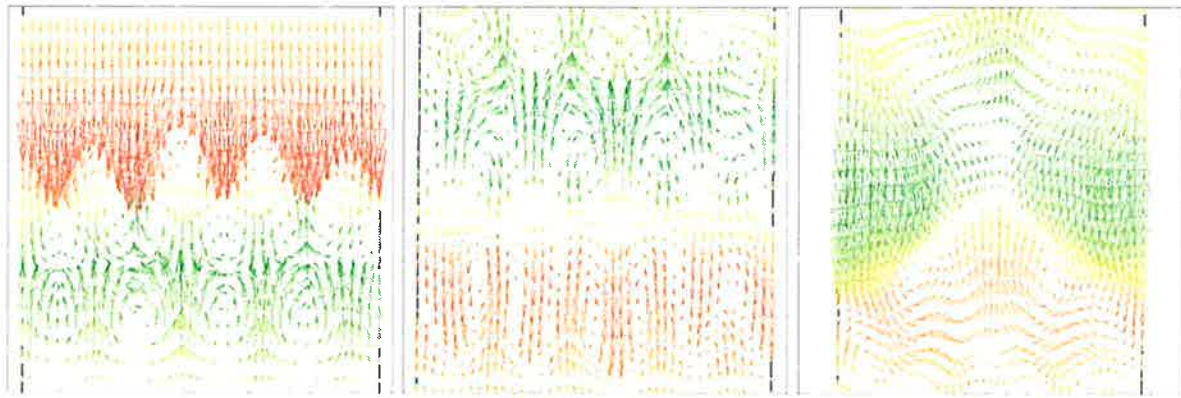


Figure 6. Flow at $Re = 300$: velocity vectors in spanwise planes at $x/d = 4.60$ (left), 6.85 (center), 11.36 (right).

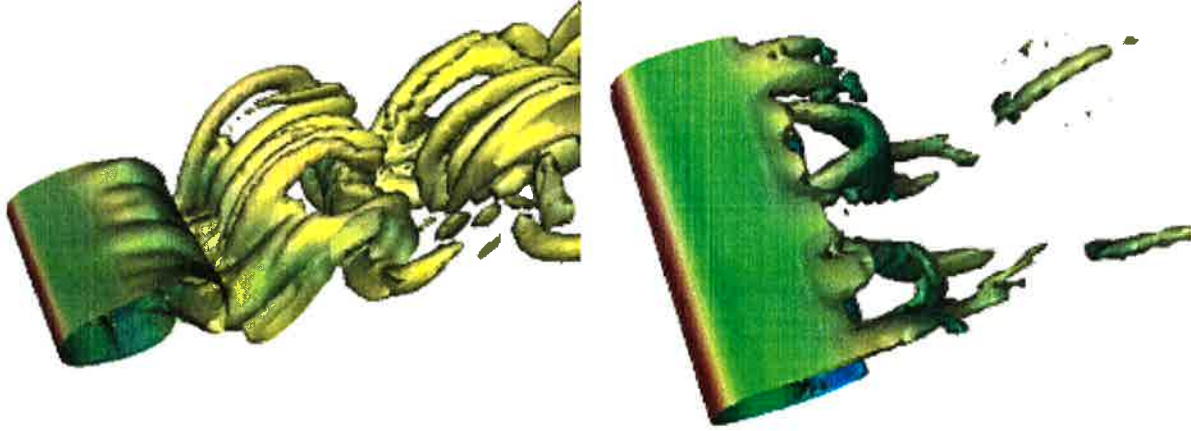


Figure 9. Flow at $Re = 800$: vorticity isosurfaces for $|\omega| = 0.5$ (left) and 2.0 (right).

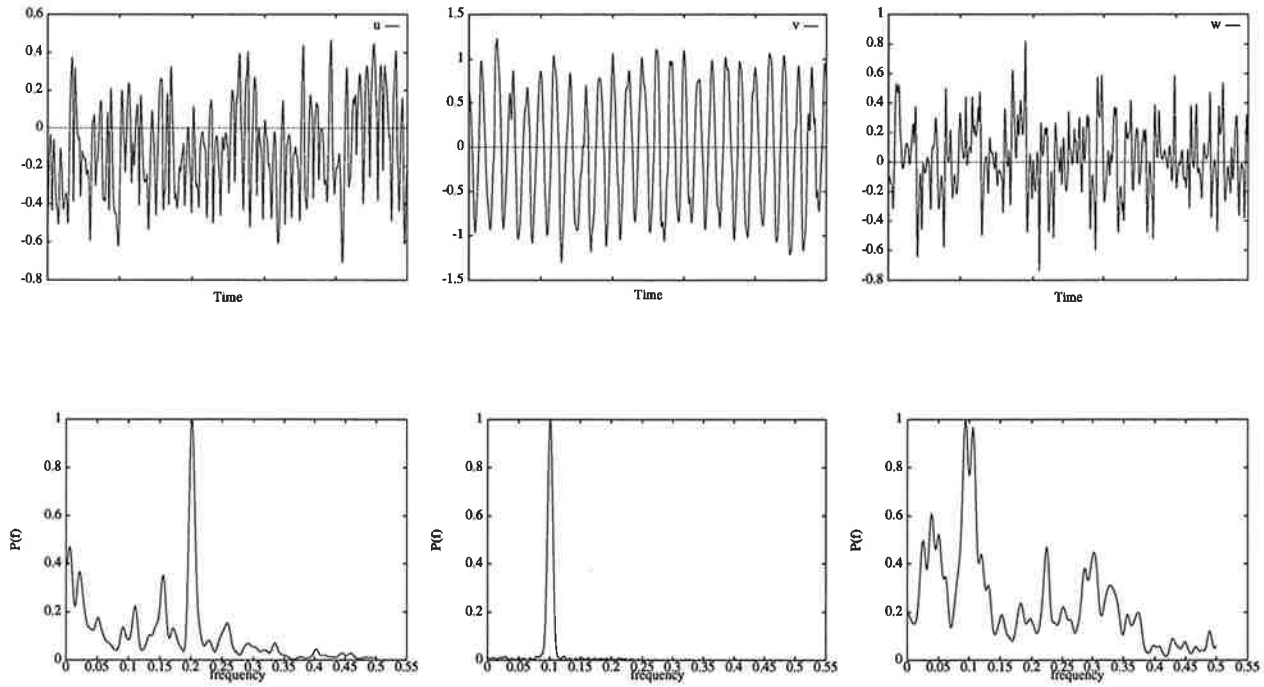


Figure 10. Flow at $Re = 800$: time-histories and power spectra of 'u', 'v', 'w' at a point downstream of the cylinder along the centerline.

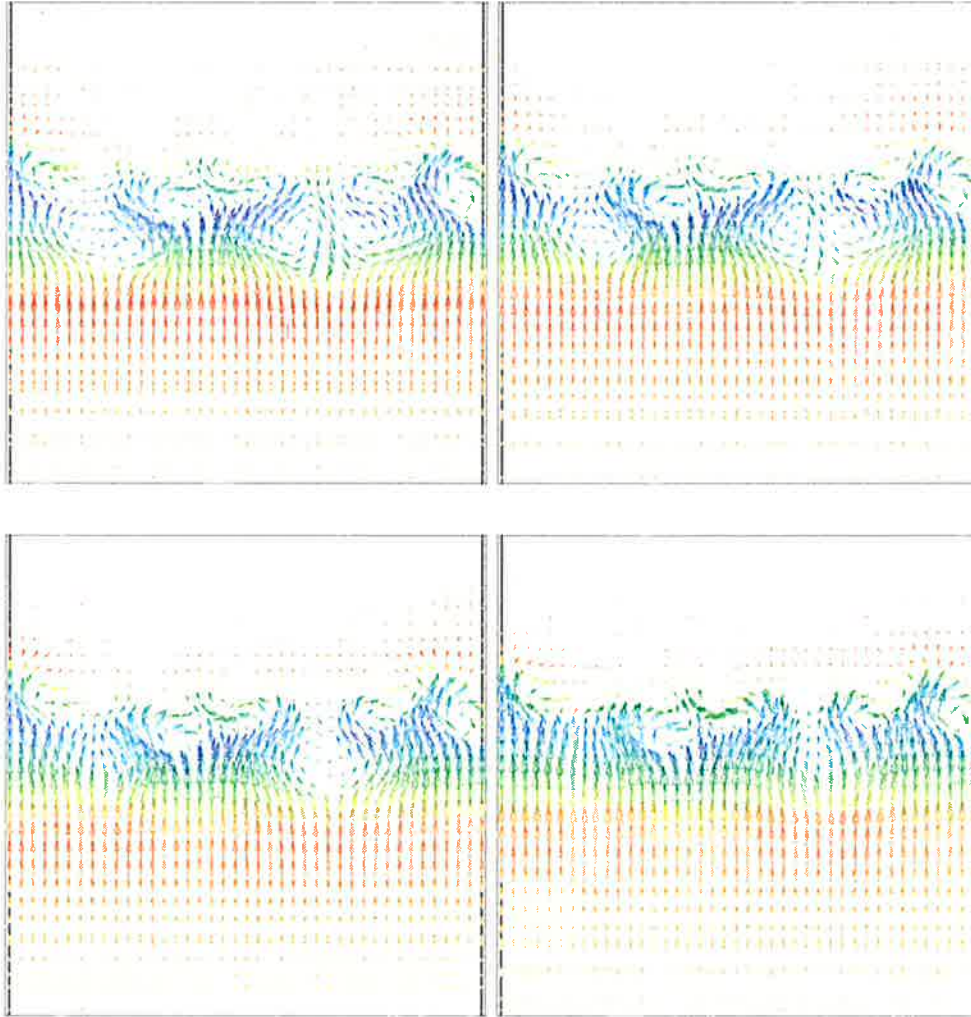


Figure 11. Flow at $Re = 800$: velocity vectors in spanwise planes $x/d = 1.15$ (top left), 1.19 (top right), 1.26 (bottom left), 1.33 (bottom right). Observe the annihilation of the counter-rotating vortex pair to the right of center.

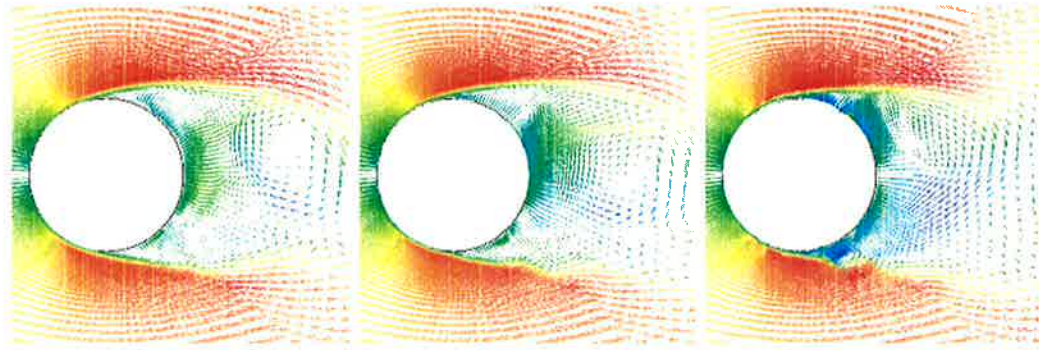


Figure 14. LES of flow at $Re=10,000$: velocity vectors in the chordwise planes at $z/d = -4.00$ (left), -1.75 (center), 4.00 (right).

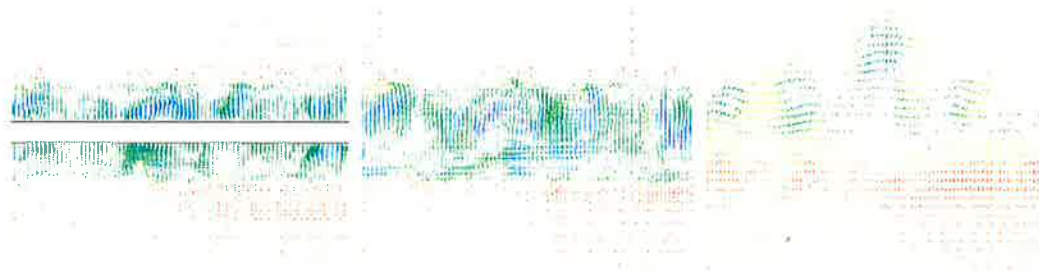


Figure 15. LES of flow at $Re=10,000$: velocity vectors in spanwise planes at $x/d = 0.96$ (left), 1.24 (center), 4.80 (right).

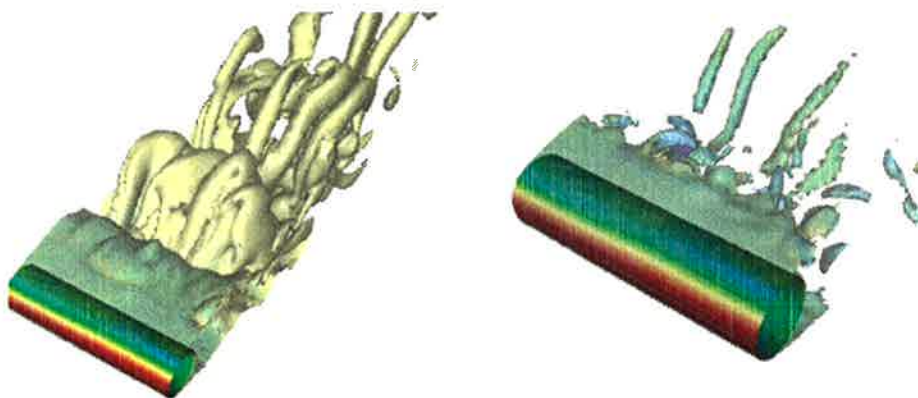


Figure 16. LES of flow at $Re=10,000$: vorticity isosurfaces for $|\omega| = 0.5$ (left) and 2.0 (right).

Visualization of the flow field in chordwise planes (perpendicular to the cylinder axis) reveals fine-scale structures. There is a clear demarcation between the turbulent wake and the laminar outer flow (see Fig. 14). We observe the turbulent formation (recirculating) region bounded by shear layers. The shear layers roll up to produce small-scale vortices at the edge of the formation zone. These vortices cause entrainment of free-stream fluid into the recirculating zone. The flow features vary significantly along the span, marked by appearance of small-scale vortices at varying locations. The flow on the cylinder separates at an angle $\sim 80^\circ$ (measured from the leading stagnation point).

Visualization of the flow in the spanwise planes also bring out the presence of the fine-scale structures (see Fig. 15). These fine-scale structures amalgamate by viscous action and only the large-scale streamwise vortices are discernible further downstream.

Fig. 16 shows the isosurfaces for two different vorticity values. The features are very similar to those from $Re = 800$; however the structures are more diffuse due to the increased turbulence.

4. Concluding remarks

With our parallel computations, we were able to capture the strongly 3D character of the wake of a circular cylinder. There were significant differences between 2D and 3D simulations at higher Reynolds numbers. For the 3D simulations, the drag coefficients and Strouhal numbers were in excellent agreement with experimental results for all cases, including the LES computations.

Acknowledgements

This research was sponsored by ARPA under NIST contract 60NANB2D1272 and by the Army High Performance Computing Research Center under the auspices of the Department of the Army, Army Research Laboratory cooperative agreement number DAAH04-95-2-0003/contract number DAAH04-95-C-0008, the content of which does not necessarily reflect the position or the policy of the government, and no official endorsement should be inferred. CRAY C90 time was provided in part by the University of Minnesota Supercomputer Institute.

References

- [1] M. Behr, A. Johnson, J. Kennedy, S. Mittal, T.E. Tezduyar, Computation of incompressible flows with implicit finite element implementations on the connection machine, *Comput. Meth. Appl. Mech. Eng.* 108 (1993) 99–118.
- [2] T. Tezduyar, S. Aliabadi, M. Behr, A. Johnson, S. Mittal, Massively parallel finite element computation of three-dimensional flow problems, *Proc. 6th Jpn. Num. Fluid Dynamics Symp.*, Tokyo, Japan, 1992, pp. 15–24.
- [3] Z. Johan, Data parallel finite element techniques for large-scale computational fluid dynamics, Ph.D. thesis, Department of Mechanical Engineering, Stanford University, 1992.

- [4] T. Tezduyar, S. Aliabadi, M. Behr, A. Johnson, S. Mittal, Parallel finite-element computation of 3D flows, *IEEE Comput.* 26 (10) (1993) 27–36.
- [5] V. Kalro, T. Tezduyar, Parallel finite element computation of 3D incompressible flows on MPPs, in: W.G. Habashi (Ed.), *Solution techniques for large-scale CFD problems*, Computational Methods in Applied Sciences, Wiley, 1995.
- [6] S. Mittal, T.E. Tezduyar, Massively parallel finite element computation of incompressible flows involving fluid–body interactions, *Comput. Meth. Appl. Mech. Eng.* 112 (1994) 253–282.
- [7] T. Tezduyar, S. Aliabadi, M. Behr, A. Johnson, V. Kalro, C. Waters, 3D simulation of flow problems with parallel finite element computations on the CRAY T3D, in: *Computational Mechanics '95*, Proc. Int. Conf. on Computational Engineering Science, Mauna Lani, Hawaii, 1995.
- [8] V. Kalro, T. Tezduyar, Parallel sparse matrix computations for finite element flow simulations on distributed memory platforms, to appear in *Proc. Int. Conf. Numerical Methods in Continuum Mechanics (NMCM)*, 1996.
- [9] T.J.R. Hughes, A.N. Brooks, A multi-dimensional upwind scheme with no crosswind diffusion, in: T.J.R. Hughes (Ed.), *Finite Element Methods for Convection Dominated Flows*, AMD, vol. 34, ASME, New York, 1979, pp. 19–35.
- [10] T.E. Tezduyar, Stabilized finite element formulations for incompressible flow computations, *Adv. Appl. Mech.* 28 (1991) 144.
- [11] Y. Saad, M. Schultz, GMRES: A generalized minimal residual algorithm for solving nonsymmetric linear systems, *SIAM J. Sci. Stat. Comput.* 7 (1986) 856–869.
- [12] J. Smagorinsky, General circulation experiments with the primitive equations, part I: the basic experiment, *Monthly Weather Rev.* 91 (1963) 99–164.
- [13] M. Germano, U. Piomelli, P. Moin, W.H. Cabot, A dynamic subgrid eddy viscosity model, *Proc. Summer Workshop, Center for Turbulence Research, Stanford, CA*, 1993.
- [14] P. Moin, J. Jimenez, Large eddy simulations of complex turbulent flows, *AIAA Paper 93-3099*, 24th Fluid Dynamics Conf., Orlando, FL, 1993.
- [15] S. Mittal, Stabilized space-time finite element formulations for unsteady incompressible flows involving fluid–body interactions, Ph.D. thesis, University of Minnesota, 1992.
- [16] M. Coutanceau, J.-R. Defaye, Circular cylinder wake configurations: A flow visualization survey, *Appl. Mech. Rev.* 44 (6) (1991) 255–305.
- [17] G.E. Karniadakis, G.S. Triantafyllou, Three-dimensional dynamics and transition to turbulence in the wake of bluff bodies, *J. Fluid Mech.* 238 (1992) 1–30.
- [18] C.H.K. Williamson, Vortex dynamics in the cylinder wake, *Annul Rev. Fluid Mech.* 28 (1996) 477–539.
- [19] A. Roshko, On the development of turbulent wakes from vortex streets, *NACA Rep.* 1191, NACA, 1954.
- [20] C.H.K. Williamson, Oblique and parallel mode of vortex shedding in the wake of a circular cylinder at low Reynolds numbers, *J. Fluid Mech.* 206 (1989) 579–627.
- [21] C.H.K. Williamson, The existence of two stages in the transition to three-dimensionality of a circular cylinder wake, *Phys. Fluids* 31 (11) (1988) 3165–3167.
- [22] Tennekes H., Lumley J.L., *A first course in turbulence*, MIT Press, 1972.
- [23] H. Schlichting, *Boundary-layer Theory*, 7th ed., McGraw-Hill, New York, 1979.
- [24] J.H. Gerard, An experimental investigation of the oscillating lift and drag of a circular cylinder shedding turbulent vortices, *J. Fluid Mech.* 11 (1961) 244–256.